ELSEVIER

Effects of initial conditions on wavelet-decomposed structures in a turbulent far-wake

Akira Rinoshika [a,*], Yu Zhou [b]

[a] *Department of Mechanical Systems Engineering, Yamagata University, 4-3-16 Jonan, Yonezawa-shi, Yamagata 992-8510, Japan*
[b] *Department of Mechanical Engineering, The Hong Kong Polytechnic University, Hung Hom, Kowloon, Hong Kong*

Abstract

The effect of initial conditions on a self-preserving plane wake has been investigated for two wake generators, i.e. a circular cylinder and a screen of 50% solidity. Measurements were made at x/θ (x is the streamwise distance downstream of the cylinder and θ is the momentum thickness of the wake) = 580 for the circular cylinder and 830 for the screen using 8 X-wires in the plane of mean shear. A vector wavelet multi-resolution technique is applied for analysis of the hot-wire data. This technique decomposes turbulent structures into a number of components based on their central frequencies, which are linked with the turbulence scales. Sectional streamlines, vorticity contours and probability density functions of the fluctuating velocities at the same central frequency, i.e. the comparable scales of turbulent structures, are examined and compared between the two generators. Discernible differences are observed in the turbulent structures of large-down to intermediate-scales. The differences are further quantified in terms of contributions from the turbulent structures of different scales to the Reynolds stresses and vorticity variance. The vorticity behavior of the screen wake is different from that of the circular cylinder. The difference exhibits an extraordinary similarity to that in the near wake.
© 2007 Elsevier Inc. All rights reserved.

Keywords: Far wake; Initial condition; Wavelet multi-resolution analysis; Turbulent structure

1. Introduction

Whether turbulence memorizes itself is a fundamentally important issue, which has received considerable attention in the literature. Experimental evidence has pointed to the persistence of initial conditions in the self-preserving region of a turbulent flow. Bevilaqua and Lykoudis (1978) compared the wake of a sphere with that of a porous disk. Both flows had the same drag and Reynolds number, $Re_h = \frac{U_\infty h}{v} = 10,000$, where U_∞ is the free stream velocity, h the characteristic height and v is the kinematic viscosity. The turbulence intensity, normalized by the maximum

velocity deficit U_1, was found to be greater in the wake of the sphere than in that of the disk. Wygnanski et al. (1986) examined experimentally the turbulent plane wakes of various generators of approximately the same drag coefficient. Their hot-wire measurements were conducted at $x/\theta = 100$–2000, where x is the streamwise co-ordinate and θ is the momentum thickness. They concluded that the normalized longitudinal turbulence intensity $\overline{u^2}$ and Reynolds shear stress $\overline{uv}$ in the self-preserving region could depend on wake generators. Other studies (George, 1989; Bonnet et al., 1986; Louchez et al., 1987; Cimbala et al., 1988; Johansson et al., 2003) have confirmed the dependence of the detailed behavior of a turbulent far-wake on initial conditions.

The persistence of the effect of initial conditions in the self-preserving region implies a dependence of the large-scale organized structures on initial conditions because of a link between these structures and self-preservation

(Bevilaqua and Lykoudis, 1978; George, 1989). This has indeed been confirmed. Using a vorticity-based detection scheme, Zhou and Antonia (1994a,b, 1995) educed large-scale vortical structures in a self-preserving wake generated by circular, triangular, square cylinder and a screen, respectively. Conditional sectional streamlines and contours of the shear stress indicated that the large-scale vortical structures in the screen wake were more asymmetrical about the vortex center than in the solid-body ones. Accordingly, the coherent contribution to the Reynolds shear stresses was appreciably larger in the screen wake than in the solid-body wakes.

Our understanding of the large-scale vortical structures has been greatly improved in the last two decades or so. This is partly attributed to the successful development of various schemes for educing these structures from the turbulent flows, such as the phase-averaging technique (Cantwell and Coles, 1983; Kiya and Matsumura, 1985), the vorticity-based technique (Hussain and Hayakawa, 1987; Zhou and Antonia, 1993), the pattern recognition technique (Giralt and Ferré, 1993) and the scheme based on critical points (Zhou and Antonia, 1994a,b). However, turbulent structures are characterized by a wide range of scales, from large-scale coherent structures to Kolmogrov length scale structures. The relatively small-scale structures, such as the secondary vortices (Wei and Smith, 1986) or longitudinal rib-like structures that occur in the saddle region, can play an important role in the wake dynamics (Hussain and Hayakawa, 1987). However, there is a lack of reliable techniques that could educe these structures from the measured or numerical data. As a result, there is limited information, mostly of qualitative description based on flow visualization (Wei and Smith, 1986; Wu et al., 1996; Williamson, 1996), on the turbulent structures other than the large-scale coherent ones. Many aspects of these structures, including their exact role in transport and relation with the large-scale structures, remain unknown or speculative. It is suspected that the turbulent structures of intermediate-scale structures may also contribute to the dependence of a self-preserving wake on the initial conditions.

The present work aims to investigate the possible effect of initial conditions on the self-preserving turbulence structures of various scales, as well as large-scale ones. The velocity data were obtained using 8 X-wires in a turbulent far wake generated by a circular cylinder and a screen of 50% solidity, respectively. The former wake generator is associated with vortex shedding, whereas the latter is not, thus defining very different initial conditions. The wavelet transform has recently emerged as a technique to analyze the turbulent structures (Argoul et al., 1989; Farge, 1992; Li, 1998; Farge et al., 1999; Lewalle et al., 2000; Li et al., 2002). Recently, the orthogonal wavelet multi-resolution technique was developed to analyze the turbulent near-wake of a circular cylinder (Rinoshika and Zhou, 2005a). This technique is capable of tracking the turbulence structures in terms of time

and frequencies, and separating the turbulence structures into a number of components based on their characteristic frequencies or scales, thus complementing conventional vortex-detection techniques, which have difficulty in identifying turbulence structures other than the large-scale ones. Sectional streamlines and vorticity contours of various scales are examined and compared between the two wake generators. The differences are quantified in terms of the contributions from the turbulence structures of different scales to the Reynolds stresses and vorticity variance. This investigation is further linked with that in the near wake (Rinoshika and Zhou, 2005b).

2. Orthogonal wavelet technique

Orthogonal wavelet analysis, which is divided into the discrete wavelet transform and wavelet multi-resolution analysis, has been previously investigated (Yamada and Ohkitani, 1990; Meneveau, 1991; Mouri et al., 1999; Farge et al., 1999; Li et al., 2002; Rinoshika and Zhou, 2005a,b). Rinoshika and Zhou (2005a) applied the latter to the analysis of a turbulent near wake. The same technique is used in this work and briefly described in this section. The algorithm for numerically calculating the discrete wavelet transform is similar to the fast Fourier transform (FFT), and a detailed description can be found in Press et al. (1992).

2.1. Discrete wavelet transform

The discrete wavelet transform is a linear and orthogonal transformation that operates on a data set whose length is an integer power of two. Like the FFT, the discrete wavelet transform can be viewed as a rotation in function space, from the physical domain to wavelet domain, where the basis functions are called as "wavelets". The wavelet bases are rather localized in both physical and frequency spaces. Various orthogonal wavelet bases have been constructed, including Meyer basis, Daubechies basis, Coifman basis, Battle-Lemarie basis, Beylkin basis, spline basis. Different wavelet basis functions may be used to emphasize different characteristics of target data sets. For example, the use of Haar basis function may highlight discontinuity in the data, and the Daubechies family may emphasize the smoothness of the data. Without losing generality, the Daubechies wavelet basis with an order of 4 (Daubechies, 1992), which is the simplest member of the Daubechies wavelet family and has only four coefficients (c_0, c_1, c_2, c_3), is used below in order to illustrate how to conduct the discrete wavelet transform.

Given a one-dimensional data matrix V^N,

$$V^N = [v_1 \quad v_2 \quad \cdot \quad \cdot \quad \cdot \quad v_{2^N}]^\mathrm{T}, \tag{1}$$

the matrix product $C^N \times V^N = V_w$ is performed, viz.

$$
\begin{bmatrix}
c_0 & c_1 & c_2 & c_3 & & & & & & \\
c_3 & -c_2 & c_1 & -c_0 & & & & & & \\
 & & c_0 & c_1 & c_2 & c_3 & & & & \\
 & & c_3 & -c_2 & c_1 & -c_0 & & & & \\
 & & & & \ddots & & & & & \\
 & & & & & \ddots & & & & \\
 & & & & & & c_0 & c_1 & c_2 & c_3 \\
 & & & & & & c_3 & -c_2 & c_1 & -c_0 \\
c_2 & c_3 & & & & & & & c_0 & c_1 \\
c_1 & -c_0 & & & & & & & c_3 & -c_2
\end{bmatrix}
\begin{bmatrix}
v_1 \\ v_2 \\ v_3 \\ v_4 \\ \cdot \\ \cdot \\ \cdot \\ v_{2^N-3} \\ v_{2^N-2} \\ v_{2^N-1} \\ v_{2^N}
\end{bmatrix}
=
\begin{bmatrix}
s_1 \\ d_1^N \\ s_2 \\ d_2^N \\ \cdot \\ \cdot \\ \cdot \\ s_{2^{N-1}-1} \\ d_{2^{N-1}-1}^N \\ s_{2^{N-1}} \\ d_{2^{N-1}}^N
\end{bmatrix}
\tag{2}
$$

where blank entries correspond to zeroes, C^N is the matrix of the wavelet basis and V_w the first transform coefficients. The superscript T in Eq. (1) denotes a transposed matrix. As indicated in the structure of the matrix C^N, two related convolution operations are carried out. The odd rows of matrix perform an ordinary convolution with coefficients c_0, c_1, c_2 and c_3 acting as a low-pass (smoothing) filter, while the even rows perform a different convolution with coefficients c_3, $-c_2$, c_1 and $-c_0$ acting as a high-pass (difference) filter. The resulting first transform coefficient matrix, V_w, consists of interlaced smooth and difference coefficients, denoted by s_i and $d_i^N (i = 1, \ldots, 2^{N-1})$. This matrix is then permuted such that the first 2^{N-1} elements are the smooth coefficients s_i and the last 2^{N-1} elements are the difference coefficients d_i^N by pre-multiplying a permuting matrix P^N, and are expressed as

The last 2^{N-1} difference elements of V_w^N, i.e. the d^N coefficients, are called the wavelet coefficients at level N.

The wavelet basis matrix C^{N-1} and the permuting matrix P^{N-1}, which are the halves of C^N and P^N, respectively, are then applied to the first 2^{N-1} smooth elements of V_w^N. The 2^{N-2} smooth s coefficients and 2^{N-2} difference d^{N-1} coefficients are generated in this operation processing, the latter coefficients corresponding to the wavelet coefficients of the hierarchical level $N - 1$. This pyramidal procedure is repeated until the last hierarchical level 1 consisting of two s coefficients is obtained. This procedure is sometimes referred to as a *pyramidal algorithm*. Therefore, the discrete wavelet transform can be expressed in matrix form by

$$
\begin{aligned}
S &= WV^N \\
&= \left[\underbrace{s_1^m, s_2^m}_{\text{level1}}, \underbrace{d_1^2, d_2^2}_{\text{level2}}, \underbrace{d_1^3, d_2^3, d_3^3, d_4^3}_{\text{level3}}, \ldots, \underbrace{d_1^N, d_2^N, \ldots, d_{2^N/2}^N}_{\text{level}N} \right]^{\mathrm{T}}
\end{aligned}
\tag{4}
$$

$$
V_w^N = P^N \times V_w =
\begin{bmatrix}
1 & & & & & & & & & \\
 & & 1 & & & & & & & \\
 & & & & \ddots & & & & & \\
 & & & & & \ddots & & & & \\
 & & & & & & \ddots & & & \\
 & & & & & & & 1 & & \\
 & 1 & & & & & & & & \\
 & & & 1 & & & & & & \\
 & & & & & \ddots & & & & \\
 & & & & & & \ddots & & & \\
 & & & & & & & & \ddots & \\
 & & & & & & & & & 1
\end{bmatrix}
\begin{bmatrix}
s_1 \\ d_1^N \\ s_2 \\ d_2^N \\ \cdot \\ \cdot \\ \cdot \\ s_{2^N/2-1} \\ d_{2^N/2-1}^N \\ s_{2^N/2} \\ d_{2^N/2}^N
\end{bmatrix}
=
\begin{bmatrix}
s_1 \\ s_2 \\ \cdot \\ \cdot \\ \cdot \\ s_{2^N/2} \\ d_1^N \\ d_2^N \\ \cdot \\ \cdot \\ \cdot \\ d_{2^N/2}^N
\end{bmatrix}
\tag{3}
$$

where S and W are discrete wavelet coefficient (or spectrum) matrix and analyzing wavelet matrix of V^N, respectively. In the *pyramidal* operation, W is usually constructed based on a cascade algorithm of an orthogonal wavelet basis function, viz.

$$W = P^1 C^1 \ldots P^{N-1} C^{N-1} P^N C^N \qquad (5)$$

In general, wavelet basis functions are chosen such that W satisfies $W^T W = I$, where I is a unit matrix. This condition enables the discrete wavelet transform to be an orthogonal linear operator and invertible. The inverse discrete wavelet transform can be simply performed by reversing the procedure, starting with the lowest level of the hierarchy, that is,

$$V^N = W^T S. \qquad (6)$$

In the present work, the Daubechies wavelet basis with an order of 20 (Daubechies, 1992), as shown in Fig. 1, is used, rather than that with an order of 4, since a higher order wavelet basis has good frequency localization and is relatively smooth. However, wavelets with lower orders (such as Daubechies wavelet with an order of 2) are a poor approximation to an ideal band-pass filter due to its poor frequency-domain characteristics, thus being unsuitable for the analysis of turbulent signals.

2.2. Orthogonal vector wavelet multi-resolution analysis

The discrete wavelet transform produces coefficients that contain information on the relative local contribution

Fig. 1. Daubechies wavelet with an order of 20. (a) Wavelet function, (b) scaling function.

of various frequency bandwidths to the transformed data instead of the frequency components of original data. In order to obtain the grouped frequency components of the transformed data, the discrete wavelet coefficient S is first decomposed into the sum of all levels:

$$
\begin{aligned}
S &= S_1 + S_2 + S_3 \cdots + S_i + \cdots + S_N \\
&= \left[s_1^m, s_2^m, 0, \ldots, 0\right]^T + \left[0, 0, d_1^2, d_2^2, 0, \ldots, 0\right]^T \\
&\quad + \left[0, 0, 0, 0, d_1^3, d_2^3, d_3^3, d_4^3, 0, \ldots, 0\right]^T \\
&\quad + \cdots + \left[0, \ldots, 0, d_1^i, d_2^i, \ldots, d_{2^i/2}^i, 0, \ldots, 0\right]^T \\
&\quad + \cdots + \left[0, \ldots, 0, d_1^N, d_2^N, \ldots, d_{2^N/2}^N\right]^T
\end{aligned}
\qquad (7)
$$

The inverse wavelet transform is then applied to the coefficient of each level and given by

$$V^N = W^T S_1 + W^T S_2 + W^T S_3 + \cdots W^T S_i + \cdots + W^T S_N, \qquad (8)$$

where term $W^T S_1$ and $W^T S_N$ represent the data components at wavelet level 1 (the lowest grouped frequency) and level N (the highest grouped frequency). This decomposition method is referred to as the wavelet multi-resolution analysis (Mallat, 1989). In fact, the wavelet component of each level is calculated using the inverse wavelet transform of the wavelet coefficients at this level, while the wavelet coefficients of other levels are made zero (Rinoshika and Zhou, 2005a). Furthermore, the sum of all wavelet components can be used to reconstruct the original data in the case of the orthogonal wavelet bases. See Newland (1993) for more details. It is well known that wavelet transform cannot achieve simultaneous time and frequency resolutions because the time-domain resolution and the frequency resolution are governed by the Heisenberg uncertainty principle, i.e. the product of the time duration and frequency bandwidth is a constant. This principle is of course also applicable in the present context. The time-frequency partition resulting from the wavelet multi-resolution analysis is long in time when capturing low-frequency structures, thus having good frequency resolution for these structures, and long in frequency when capturing high-frequency structures, thus having good time resolution for these structures. The wavelet multi-resolution technique intelligently adapts itself to capture structure features across a wide range of frequencies, which cannot be achieved by conventional band-pass filtering techniques, and computation is faster, compared to the conventional matching techniques.

Because the number of wavelet coefficients is less than that of the original data, the degrees of freedom associated with wavelet components obtained from the inverse wavelet transform of the wavelet coefficients should be fewer than that associated with the original time series.

The wavelet multi-resolution analysis, introduced above, deals with scalar data. Since data to be analyzed are sometimes given as vectors such as velocity vectors in
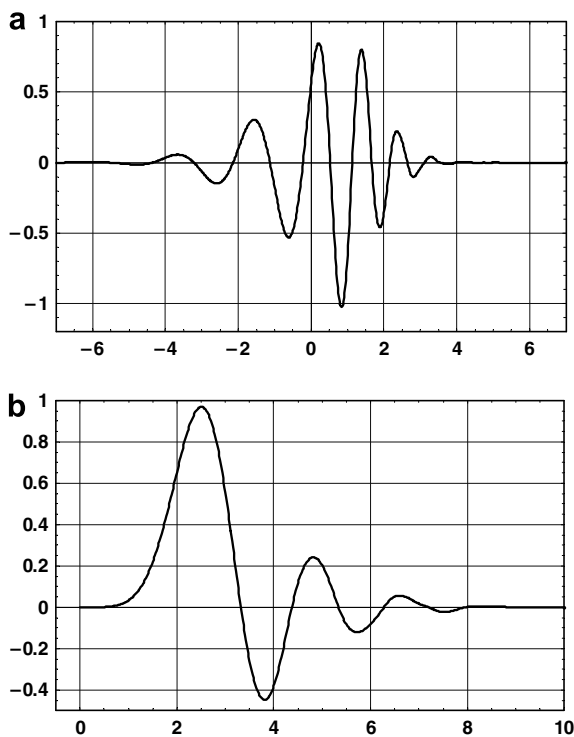
a turbulent flow field, the present investigation has extended the analysis technique to deal with vector data, referred to as the vector wavelet multi-resolution technique, which has been given little attention previously.

For a vector $\vec{v}$, the wavelet multi-resolution analysis is first performed for each component of $\vec{v}$. The wavelet component of the vector is then constructed from all the vector components of the same characteristic frequency. Thus, vector data are converted to a summation of vector wavelet components at different characteristic frequencies, viz.

$$\vec{v} = \sum_{i=1}^{N} \vec{v}_i = \sum_{i=1}^{N} \boldsymbol{W}^{\mathrm{T}} \vec{\boldsymbol{S}}_i, \tag{9}$$

where the vector wavelet components are normal to each other. In Eq. (9), $\vec{v}_1$ and $\vec{v}_N$ represent the vector wavelet components at level 1 (the lowest frequency) and level N (the highest frequency), respectively. Evidently, the sum of all vector wavelet components, i.e. Eq. (9), is a reconstruction of the original vector function.

3. Experimental conditions

Experiments were carried out in an open-return low-turbulence wind tunnel with a 2.4 m-long working section (0.35 m × 0.35 m) in Professor R.A. Antonia's laboratory at The University of Newcastle. The bottom wall was tilted to achieve a zero streamwise pressure gradient. Fig. 2 shows the experimental arrangement. A circular cylinder ($h = 6.35$ mm) and a screen ($h = 8.0$ mm) of 50% solidity were used to generate the wake, respectively, each installed in the mid-plane, 0.20 m from the exit plane of the contraction. The two generators spanned the full width of the working section, resulting in a blockage of 1.8% and

Fig. 2. Experimental arrangement.

Table 1
Characteristic wake parameters

Wake generator	h (mm)	θ (mm)	Re_h	Re_θ	L (mm)	U_1/U_∞ (%)	x/h	x/θ
Cylinder	6.35	3.0	2800	1350	25	6.9	280	580
Screen	8.00	2.1	3600	900	21	6.3	220	830

1.2%, respectively. Measurements were made at $U_\infty = 6.7$ m/s. Table 1 summarizes the characteristic flow parameters for the two wake generators, where L is the mean velocity half width, U_1 is the centerline velocity deficit and Re_θ is the Reynolds number based on θ. Zhou and Antonia (1995) confirmed that the wake was approximately self-preserved in terms of mean velocity, second moments and power spectral density function at $x/\theta = 580$ behind a circular cylinder and at $x/\theta = 830$ behind a screen. Wygnanski et al. (1986) argued that the momentum thickness was the appropriate length scale for a small deficit wake. Ideally, the measurements should have been made for the same blockage ratio and drag (Bevilaqua and Lykoudis, 1978; Wygnanski et al., 1986; Cannon et al., 1993). This would be difficult to achieve. In order to minimize the possible effect of different drag on the wake, the momentum thickness is used as the length scale for normalization in the paper. The difference in drag further results in different Reynolds number between the two wakes. However, the far wake is unlikely to depend strongly on Re_h or Re_θ. Zhou et al. (1998) investigated the dependence of the streamwise fluctuating velocity on Re_θ. As evident in their Fig. 2, the difference in the fluctuating velocity was only appreciable when a change in Re_θ exceeded 1000. Furthermore, the results presented in this paper will be either normalized by the maximum velocity deficit or the maximum variance of fluctuating velocities, which acts to minimize further the possible Re_θ effect. Therefore, a difference of 500 in Re_θ should correspond to a negligible effect in the far wake. The Kolmogorov length scale η was about 0.45 mm for both wakes.

A rake of eight X-wires, which was aligned in the plane of mean shear, i.e. the (x, y)-plane, was used to measured velocity fluctuations u and v simultaneously at eight points. The nominal spacing between X-wires was about 5 mm. Wollaston (Pt-10% Rh) wires, 5 μm in diameter and about 1 mm in working length, were operated with constant temperature circuits. Signals from the circuits were offset, amplified and then digitized using 16 channel (12 bit) A/D boards and a personal computer at a sampling frequency of $f_s = 3.5$ kHz per channel (the cut-off frequency was 1.6 kHz). The wires were calibrated for velocity and yaw, and continuously checked for drift. There was no appreciable drift observed since sampling of each set of data was about 38 s and the total duration for the acquisition of a number of sets of data was completed in a few minutes. The sampled data were processed based on velocity and yaw calibrations to obtain signals proportional to u and v, together with the local mean velocities $\overline{U}$ and $\overline{V}(\approx 0)$.
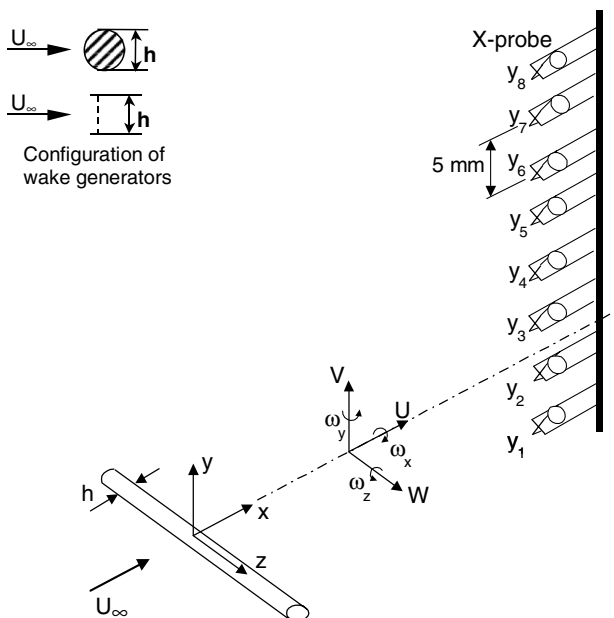
4. Decomposition of turbulent structures into various scales

4.1. Spectral characteristics of velocity fluctuations

Fig. 3 presents the power spectral density function F_u of the u-signal and F_v of the v-signal. Note that F_u (Fig. 3a) does not show any pronounced peak, but F_v (Fig. 3b) does around the frequency $f_0^* = \frac{f_0\theta}{U_1} \approx 0.41$ for the circular cylinder and 0.49 for the screen, indicating the occurrence of large-scale vortical structures. Both u- and v-spectrum display appreciable difference between the generators over a range of frequencies around f_0^*, reconfirming the connection between the turbulence memory effect and large-scale structures (Bevilaqua and Lykoudis, 1978; George, 1989; Zhou and Antonia, 1994a,b, 1995) and further suggesting a contribution from the structures of other scales, in particular intermediate scales, to the persistence of the initial conditions. The difference diminishes for the frequencies of about $4f_0^*$ and higher. It is worth pointing out that F_u (Fig. 3a) for $f < f_0$ has a quite significant magnitude, compared with that around f_0. In contrast, F_v (Fig. 3b) for $f < f_0$ is very small. This will be discussed further in Section 6.

4.2. Spectral characteristics of wavelet components

A vector wavelet multi-resolution technique is used to analyse the measured velocity data. The dominant frequency f_0 of large-scale structures, as evident in the v-spectrum (Fig. 3b), is selected as the 'fundamental frequency'. In order to determine the characteristics of each wavelet component, the thirteen wavelet components of v signals at $y/L = 0.6$ ($y/\theta = 5$ for the circular cylinder and 7 for screen) near the vortex path are analyzed by Fourier analysis. The spectrum of each wavelet component displays a peak at its central frequency and covers a range of frequencies, as illustrated in Fig. 4 at wavelet level 9 for both generators. Table 2 shows the central frequencies and their bandwidths of the wavelet components from $f_0/2$ to $8f_0$, which cover the range of frequencies that are of major concern in the present investigation. Evidently, the wavelet component of the central frequency f_0 is representative of large-scale vortical structures, and those at a multiple of f_0 and at a frequency smaller than f_0 correspond to smaller-scale and larger-scale structures, respectively. Thus, comparison between the comparable-scale turbulence structures of the two wakes may be reduced to that between the wavelet components of the same multiple f_0.
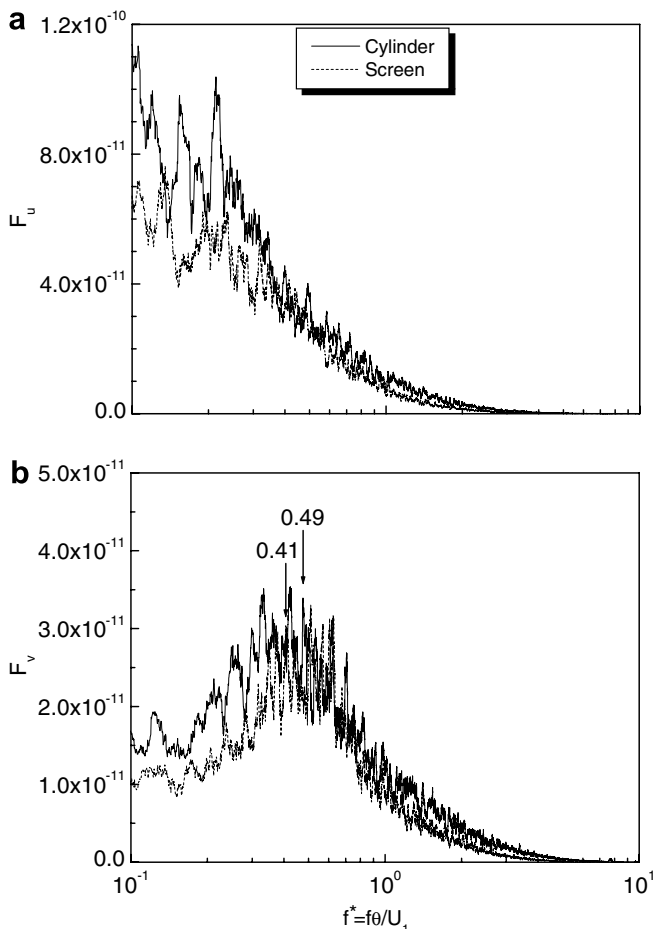
Fig. 3. (a) The u-spectrum; (b) the v-spectrum ($y/\theta \approx 5.4$ for circular cylinder and $y/\theta \approx 7.3$ for screen).
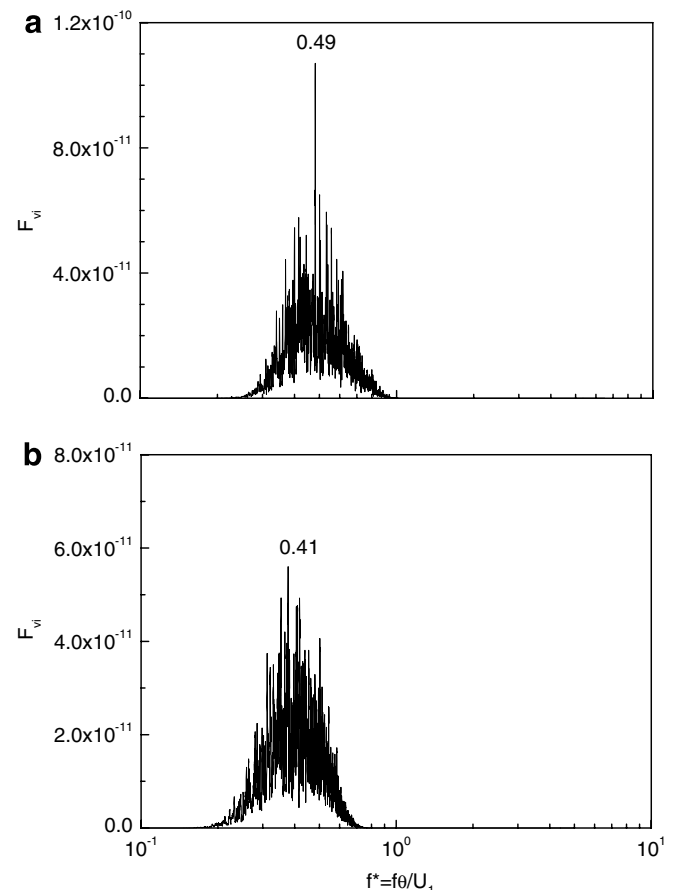

Fig. 4. The v-spectrum of the wavelet component at f_0 (wavelet level 9): (a) circular cylinder at $y/\theta \approx 5.4$, (b) screen at $y/\theta \approx 7.3$.

Table 2
Central frequencies and bandwidths of wavelet components

Wavelet level	Circular cylinder		Screen	
	Central frequencies (Hz)	Frequency bandwidth (Hz)	Central frequency (Hz)	Frequency bandwidth (Hz)
8	38 ($1/2f_0$)	20–70	42 ($1/2f_0$)	15–80
9	75 (f_0)	40–140	83 (f_0)	40–160
10	150 ($2f_0$)	80–270	160 ($2f_0$)	80–270
11	300 ($4f_0$)	110–650	330 ($4f_0$)	110–650
12	600 ($8f_0$)	220–1100	660($8f_0$)	220–1100

4.3. Vorticity approximation

Vorticity approximation may be obtained based on velocity data using the central difference approximation (Zhou and Antonia, 1993). As such, the eight X-wires in the (x, y)-plane may produce spanwise vorticity data at each of the seven midpoints between adjacent X-wires. The spanwise vorticity component of the ith wavelet component may be approximated by

$$\omega_{zi} = \frac{\partial V_i}{\partial x} - \frac{\partial U_i}{\partial y} = \frac{\partial v_i}{\partial x} - \frac{\partial(\overline{U} + u_i)}{\partial y} \approx \frac{\Delta v_i}{\Delta x} - \frac{\Delta(\overline{U} + u_i)}{\Delta y},$$
(11)

where $\Delta y (\approx 5.0\ mm)$ is spacing between two X-wires in the (x, y)-plane; $\Delta x = -\overline{U}\Delta t$ (Taylor's hypothesis) $= -\overline{U}/f_s$. For simplicity, $U_c = 0.94U_\infty$ on the vortex path (Zhou and Antonia, 1995) is used to calculate Δx. Vorticity con-

tours and root mean square (rms) values thus obtained showed no appreciable difference from those obtained using local mean velocity. Note that vorticity is indirectly calculated from velocity signals using the central difference approximation. Spacing between X-wires is about 5 mm, significantly larger than the Kolmogorov length (≈ 0.45 mm) at the centerline, implying an insufficient spatial resolution of vorticity. Because there is a lack of reliable vorticity data for this flow in the literature, it is difficult to translate reliably the inadequate resolution into errors caused. However, the approximation is relatively easy to implement and should be adequate for describing at least the relatively large- and intermediate-scale vorticity field, thus providing useful qualitative information on the relationship between different wavelet components. But it should be cautioned that the vorticity estimate for relatively small-scale structures might not be trustworthy.

5. Turbulent structures of different wavelet components

Sectional streamlines (Williamson, 1996), hereafter referred to as streamlines for brevity, were constructed from the velocity vectors of measured velocity or wavelet components to 'visualize' the flow structure. Fig. 5 shows instantaneous streamlines and the contours of normalized vorticity, $\omega_z\theta/U_1$, from measured data for both generators. To avoid the distortion of flow patterns, the same scales have been used for $\frac{x}{\theta} = -\frac{tU_c}{\theta}$ and $\frac{y}{\theta}$ in both streamlines and vorticity contours. Large-scale vortical structures are evident in streamlines, though the structures of other scales
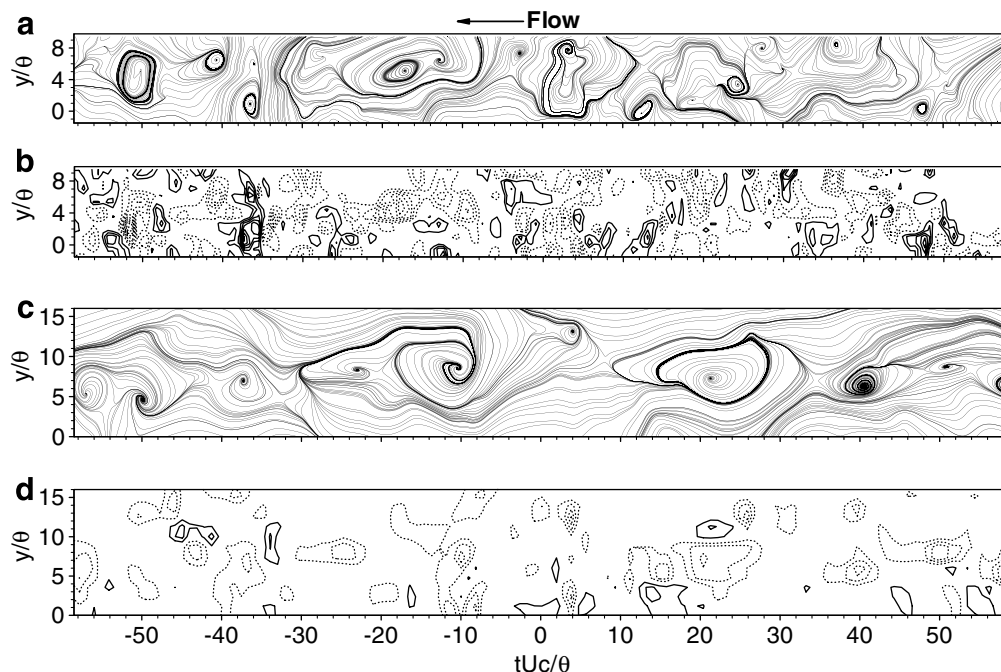

Fig. 5. Circular cylinder: (a) measured instantaneous sectional streamlines; (b) vorticity contours, $\omega_z\theta/U_1$ (Max: 0.07, Min: −0.09, increment: 0.01). Screen: (c) measured instantaneous sectional streamlines; (d) vorticity contours, $\omega_z\theta/U_1$ (Max: 0.04, Min: −0.04, increment: 0.01). Solid and broken lines in (b) and (d) represent positive and negative contours, respectively. The contour levels of $|\omega_z|\theta/U_1 \leqslant 0.01$ have been removed. The origin of time is arbitrary.

are also identifiable. However, it would be difficult to study the behaviors of the structures other than the large-scale ones for either flow based on Fig. 5. In general, the vortical structure centers shown in streamlines coincide with the local vorticity peaks, suggesting that information about the flow structure may be obtained by examining either streamlines or vorticity.

Fig. 6 presents the vorticity contours and streamlines, calculated from the wavelet components of velocity at the central frequency f_0, which is likely representative of coherent structures. The foci and saddle points in Fig. 6 are in general approximately coincident with those in Fig. 5 but appear better defined. To facilitate data interpretation, these points are marked by 'F' and 'S', respectively, on the upper side of the streamlines of the wavelet component at f_0 in Fig. 6 and those at $2f_0$ in Fig. 7. The streamlines and vorticity contours (Fig. 6) of the wavelet component at f_0 display clearly four quasi-periodical vortical structures for both wakes, corresponding well to the large-scale structures in Fig. 5. Furthermore, the flow structure appears rather similar to the conditionally averaged results based on the detections of large-scale structures (Zhou and Antonia, 1994a,b, 1995) thus providing a validation of the data analysis technique presently used. Apparently, there is a correspondence between the wavelet component of the central frequency f_0 and the large-scale vortices. It is perhaps difficult to identify a qualitative difference in the flow struc-

ture between the two wake generators. But the vortical structures in the circular cylinder are associated with higher vorticity concentrations (Fig. 6b) than those (Fig. 6d) in the screen wake. Furthermore, there is appreciable 'intrusion' by positive $(\omega_z)_{f_0}\theta/U_1$ at $tU_c/\theta \approx -43 \sim -26$ and $-16 \sim 1$ above the centerline in the cylinder wake. These positive vorticity concentrations occur in the saddle region and seem to show a tendency aligned along the converging separatrix (Hussain and Hayakawa, 1987). As a matter of fact, these concentrations are identifiable in the contours (Fig. 5b, $tU_c/\theta \approx -40 \sim -35$ and $-5 \sim 1$) of spanwise vorticity derived from the measured velocities. In contrast, such 'intrusion' is almost nonexistent in the screen wake. Interestingly, the same difference occurs in the near wake (see Rinoshika and Zhou, 2005b), though the positive $(\omega_z)_{f_0}\theta/U_1$ contours did not appear aligned along the converging separatrix in the cylinder near-wake. The observation between the cylinder and screen wakes is likely linked with a difference in spanwise vortex strength between the two flows. The maximum magnitude of negative $(\omega_z)_{f_0}\theta/U_1$ associated with spanwise vortices above the centerline is -0.022 in the cylinder wake, almost twice that (-0.014) in the screen wake (Fig. 6b). A similar difference is observed in the near wake (Rinoshika and Zhou, 2005b). The strong vortices should correspond to a strong straining motion in the saddle region, which is likely responsible for the occurrence of
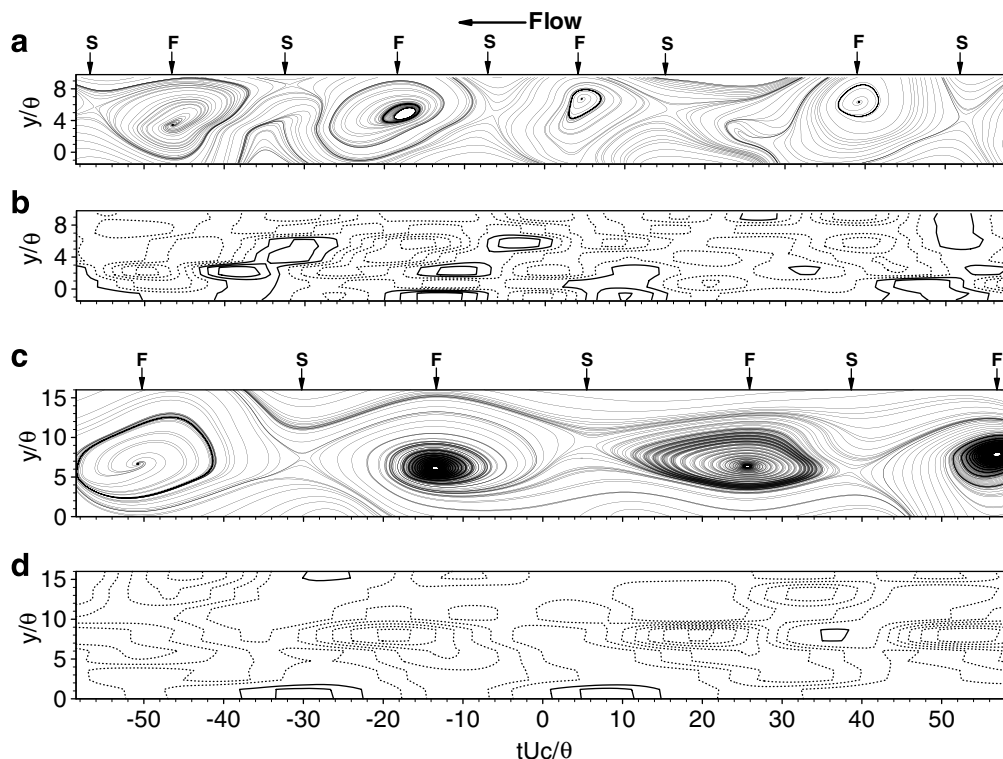

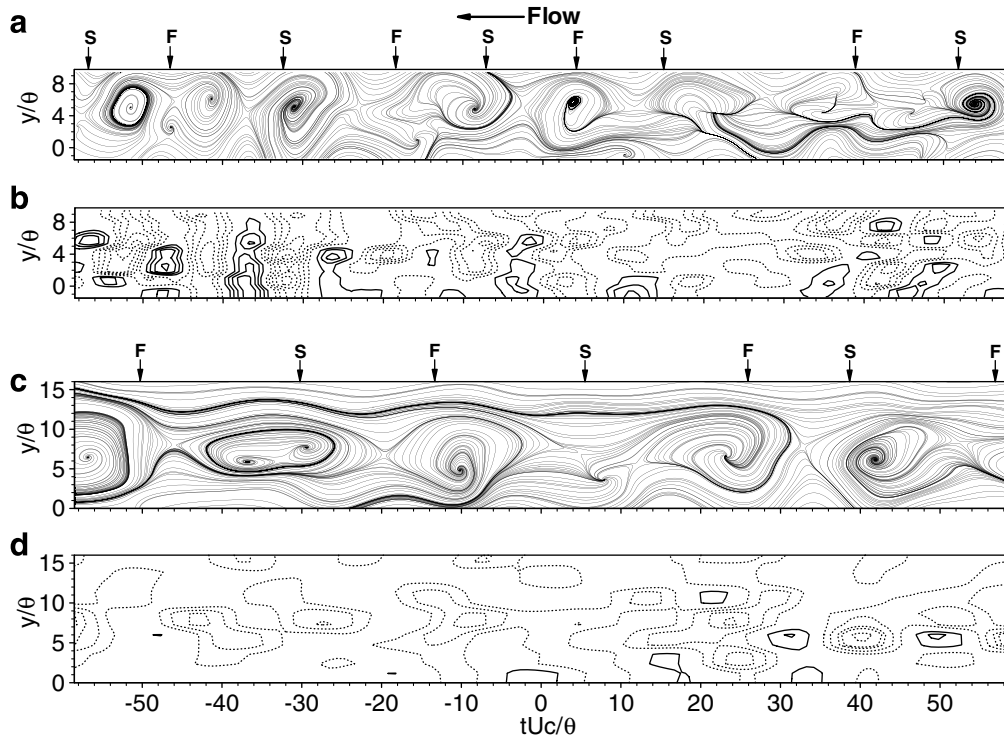Fig. 6. Circular cylinder: (a) sectional streamlines of the wavelet component at f_0; (b) vorticity contours, $(\omega_z)_{f_0}\theta/U_1$ (Max: 0.014, Min: -0.022, increment: 0.004). Screen: (c) sectional streamlines of the wavelet component at f_0; (d) vorticity contours, $(\omega_z)_{f_0}\theta/U_1$ (Max: 0.006, Min: -0.014, increment: 0.002). Solid and broken lines in (b) and (d) represent positive and negative contours, respectively. The contour levels of $(\omega_z)_{f_0}\theta/U_1 \leqslant 0.002$ have been removed. The origin of time is arbitrary.

Fig. 7. Circular cylinder: (a) sectional streamlines of the wavelet component at $2f_0$; (b) vorticity contours, $(\omega_z)_{2f_0}\theta/U_1$ (Max: 0.016, Min: −0.024, increment: 0.004). Screen: (c) sectional streamlines of the wavelet component at $2f_0$; (d) vorticity contours, $(\omega_z)_{2f_0}\theta/U_1$ (Max: 0.012, Min: −0.018, increment: 0.004). Solid and broken lines in (b) and (d) represent positive and negative contours, respectively. The contour levels of $(\omega_z)_{2f_0}\theta/U_1 \leqslant 0.004$ have been removed. The origin of time is arbitrary.

the positive $(\omega_z)_{f_0}\theta/U_1$ concentrations. Note that such positive concentrations are not always associated with saddle points, e.g. at $tU_c/\theta \approx 16$, suggesting that the orientation of the structures in the saddle region could be quite arbitrary.

As the central frequency increases to $2f_0$ (Fig. 7), the structures occur more frequently but show a smaller size than those in Fig. 6. Some of them are apparently associated with the vortical structures at f_0, for example, at $tU_c/\theta \approx 5$ in the circular cylinder wake and at $tU_c/\theta \approx -10$ and 24 in the screen wake. More occur in

the saddle region between the large-scale vortices, for example, at $tU_c/\theta \approx -31$, −8, 18 and 54 for the cylinder and −37, −30 and 42 for the screen. The latter observation is consistent with the occurrence of longitudinal or rib structures (Rinoshika and Zhou, 2005a), which occur between successive spanwise structures (Cantwell and Coles, 1983; Zhou and Antonia, 1993). A more frequent occurrence of the latter structures suggests that the rib-structures could make a predominant contribution to the wavelet component of $2f_0$. Note that some of these intermediate-scale structures are also identifiable in the measured
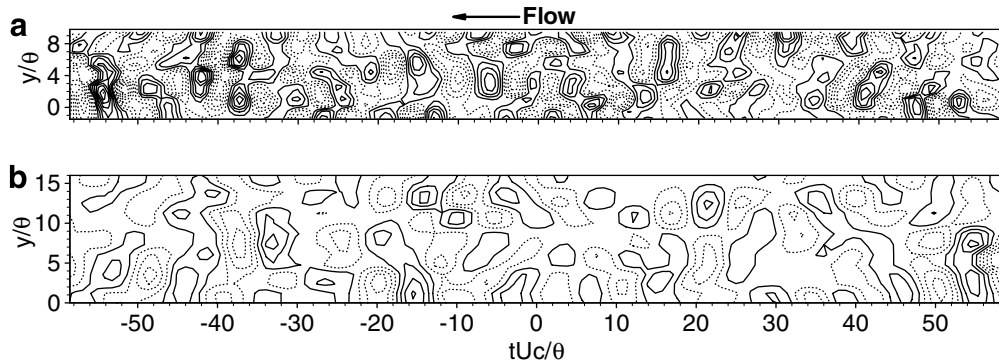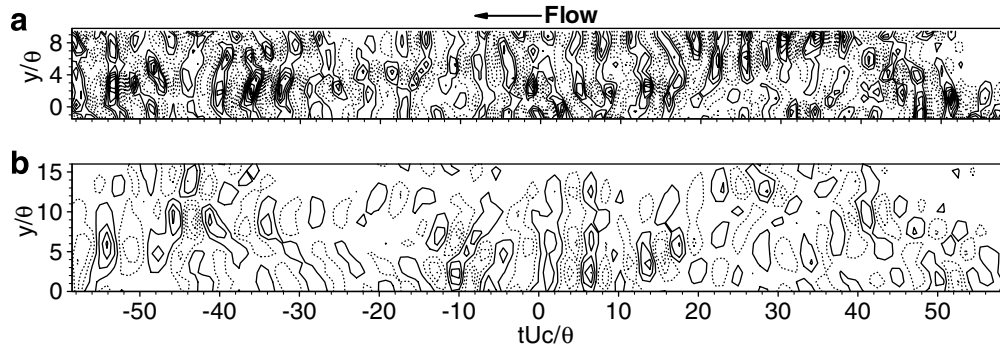

Fig. 8. Vorticity contours of the wavelet component at $4f_0$, $(\omega_z)_{4f_0}\theta/U_1$: (a) circular cylinder (Max: 0.03, Min: −0.026, increment: 0.004); (b) screen (Max: 0.014, Min: −0.018, increment: 0.004). Solid and broken lines represent positive and negative contours, respectively. The contour levels of $(\omega_z)_{4f_0}\theta/U_1 \leqslant 0.002$ have been removed. The origin of time is arbitrary.

data, e.g. the structures at $tU_c/\theta \approx -52$ and -51 for cylinder (Fig. 5a) and $tU_c/\theta \approx -57$ for screen (Fig. 5c), demonstrating that the wavelet technique presently used can indeed separate the turbulence structures of different scales. Similarly to the case of f_0, the positive $(\omega_z)_{2f_0}\theta/U_1$ concentrations occur more frequently in the cylinder wake

(Fig. 7b) than in the screen wake (Fig. 7d). Furthermore, these concentrations generally occur in the saddle between consecutive structures at $2f_0$, e.g., at $tU_c/\theta \approx -57$, -46 and -2. The observation is again probably attributed to the larger strength of structures at $2f_0$ in the cylinder wake than in the screen wake; the maximum magnitude of negative

Fig. 9. Vorticity contours of the wavelet component at $8f_0$, $(\omega_z)_{8f_0}\theta/U_1$: (a) circular cylinder (Max: 0.026, Min: -0.03, increment: 0.004); (b) screen (Max: 0.014, Min: -0.018, increment: 0.004). Solid and broken lines represent positive and negative contours, respectively. The contour levels of $(\omega_z)_{8f_0}\theta/U_1 \leqslant 0.002$ have been removed. The origin of time is arbitrary.
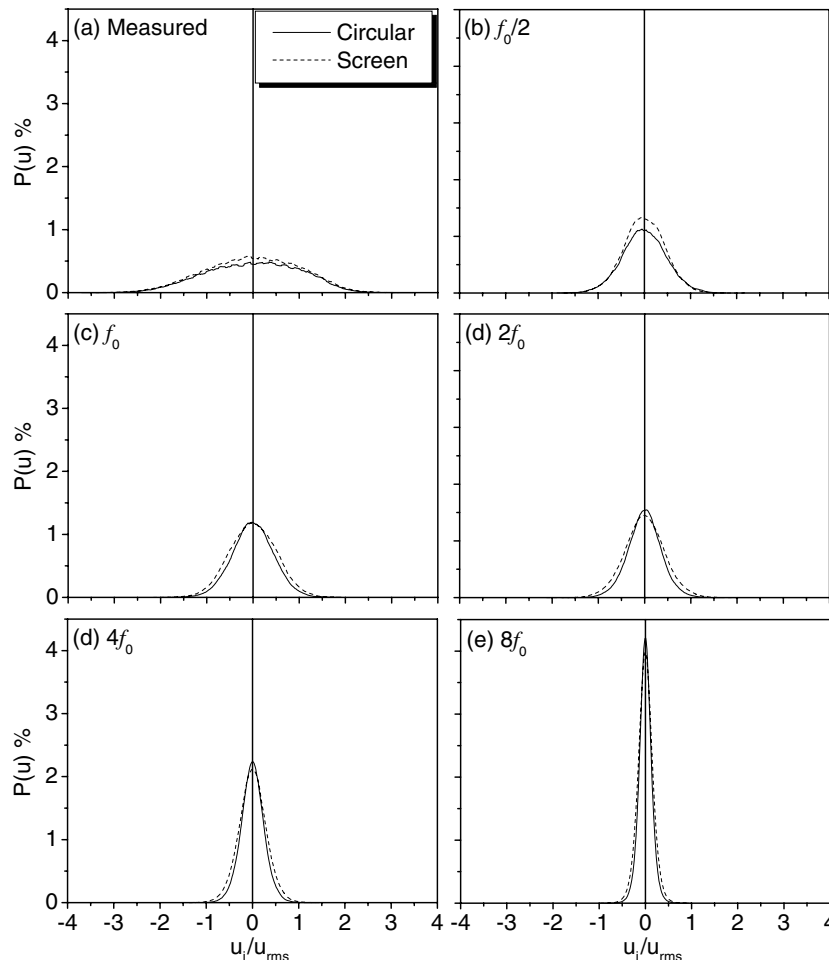
Fig. 10. Probability density functions, $P(u)$, of the measured and the wavelet components for u-component at various central frequencies ($y/\theta \approx 7.0$ for circular cylinder and $y/\theta \approx 7.3$ for screen).

$(\omega_z)_{2f_0} \theta/U_1$ in the two wakes is about 0.024 and 0.018, respectively.

Vorticity contours of the wavelet components at $4f_0$ and $8f_0$ (Figs. 8 and 9) do not seem to be correlated with foci and saddle points associated with the vortical structures of f_0. This implies that the characteristics of the small-scale components are not in phase locked with the large-scale components. (Steamlines were not constructed for the wavelet components of central frequencies higher than $2f_0$ since the convection velocity U_c of large-scale structures, at which the reference frame of streamlines is translated, may not be appropriate for relatively small-scale structures.) The vorticity contours appear elongated laterally, particularly at $8f_0$ and tend to show vorticity concentrations of alternate sign along the flow direction. Vorticity concentrations in the cylinder wake are appreciably stronger than in the screen wake; the maximum magnitude of $(\omega_z)_{4f_0} \theta/U_1$ or $(\omega_z)_{4f_0} \theta/U_1$ is 0.26 for the cylinder but 0.18 for screen.

The wavelet components at a central frequency higher than $8f_0$ are not shown because of their diminishing contribution to measured vorticity and Reynolds stresses (see Section 6).

Figs. 10 and 11 present the probability density functions, $P(u)$ and $P(v)$, of u and v and their wavelet components. The signals u and v were measured at $y/\theta \approx 7$, which corresponds approximately to the most likely path of large-scale vortical structures. A difference is discernible in the measured $P(u)$ (Fig. 10a) between the two wakes, which is largely attributed to the wavelet components of $\frac{1}{2}f_0$ (Fig. 10b) and lower frequencies. The measured $P(v)$ (Fig. 11a) for the two wakes almost collapses together. However, there is a marked difference in their wavelet components of the central frequency up to $4f_0$. $P(v)$ at f_0 (Fig. 11c) and $\frac{1}{2}f_0$ (Fig. 11b) spreads more on both sides, implying a larger fluctuating lateral velocity, for cylinder than for screen. The observation is consistent with the significantly higher maximum vorticity concentration $((\omega_z)_{f_0} \theta/U_1 = -0.022$, Fig. 6b) in the cylinder wake than that (-0.014) in the screen wake. But an opposite observation is made for $P(v)$ at $2f_0$ (Fig. 11d) and $4f_0$ (Fig. 11e); $P(v)$ exhibits a more pronounced peak at $v_i/v_{rms} = 0$ for cylinder. Correspondingly, the maximum $(\omega_z)_{2f_0} \theta/U_1$ (Fig. 7b) increases, compared with that of $(\omega_z)_{f_0} \theta/U_1$ (Fig. 6b), about 10% in the cylinder wake, but 30% in the screen wake. $P(v)$ at $8f_0$ (Fig. 11f) is virtually identical for two wake generators, reconfirming the negligi-
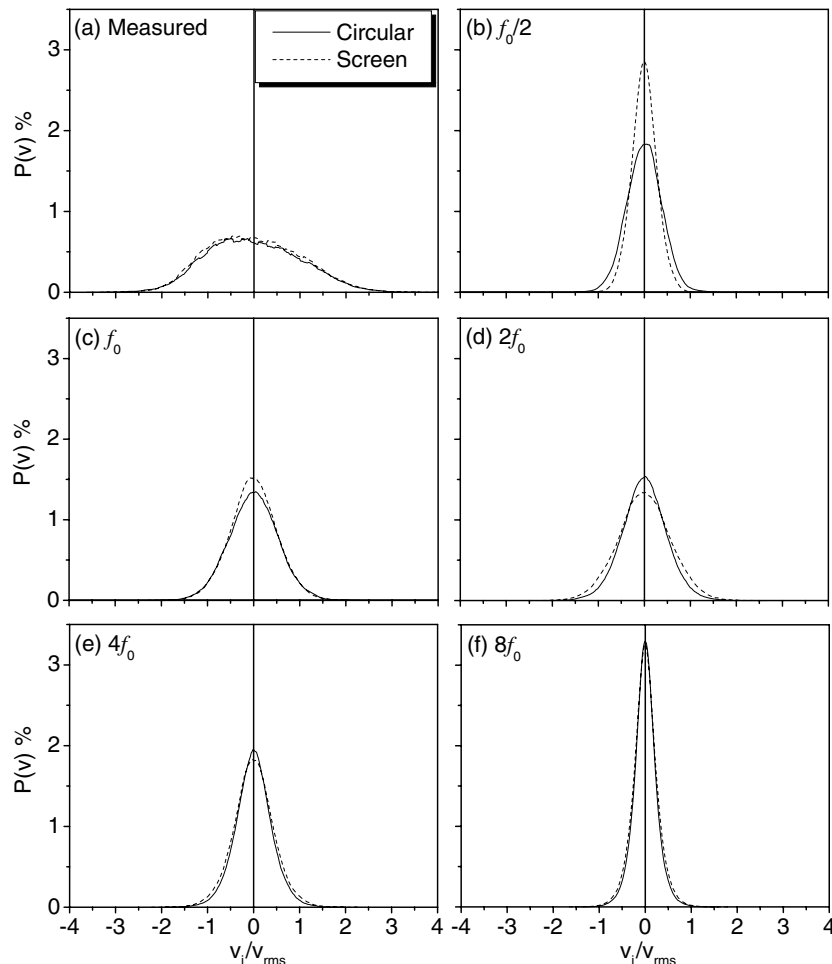

Fig. 11. Probability density functions, $P(v)$, of the measured and the wavelet components for v-component at various central frequencies ($y/\theta \approx 7.0$ for circular cylinder and $y/\theta \approx 7.3$ for screen).

ble effect of initial conditions on the small-scale structures of $8f_0$ or higher frequencies.

6. Contribution from turbulent structures of different scales to Reynolds stresses and vorticity variance

The time-averaged product of the wavelet components β_i and γ_i, each representing u_i, v_i or ω_{zi}, may be calculated by

$$\overline{\beta_i\gamma_i} = \frac{1}{n}\sum_{j=1}^{n}\beta_i(t_j)\gamma_i(t_j), \qquad (12)$$

where $n = 133,000$, which is the total number of measured data points. The product is normalized by the maximum value of the measured time-averaged product $(\overline{\beta\gamma})_{max}$ to indicate the contribution from each wavelet component, i.e. the turbulent structures of a range of scales, to the Reynolds stresses or vorticity variance. This information is of fundamental importance and also valuable for numerical modeling.

Fig. 12 presents time-averaged Reynolds stresses and the wavelet components of central frequencies from $\frac{1}{2}f_0$ up to

$8f_0$. Fig. 13 is also given to show more clearly the dependence of the wavelet components on the central frequency. The wavelet components at a central frequency lower than $\frac{1}{2}f_0$ do not seem to be physically important; on the other hand, those at a frequency higher than $8f_0$ contribute about 1% or even smaller to Reynolds stresses. Therefore, the components whose central frequency falls below $\frac{1}{2}f_0$ or above $8f_0$ are not shown. The negative $\overline{u_iv_i}/(\overline{uv})_{max}$ near $y/L = 0$ and at relatively high central frequencies has been removed in Fig. 12c to allow the log-scale presentation. The $(\overline{\beta\gamma})_{max}$ values (Table 3) show discernible difference between the cylinder and screen wakes. The observation is agreeable with Zhou and Antonia's report (1995), suggesting the effect of different generators on Reynolds stresses and vorticity variance.

The total contribution from the components of $\frac{1}{2}f_0$, f_0, $2f_0$, $4f_0$ and $8f_0$ accounts for about 80% of $\overline{u^2}$, 96% of $\overline{v^2}$ and 97% of $\overline{uv}$. The five components are reasonably representative of the flow in terms of $\overline{v^2}$ and $\overline{uv}$, but not so in $\overline{u^2}$. It has been verified that errors caused by neglecting the components whose central frequency exceeds $8f_0$ are negligible. The u-spectrum (Fig. 3a) exhibits significant energies at frequencies lower than $\frac{1}{2}f_0$, that is, the deficit between $\overline{u^2}$
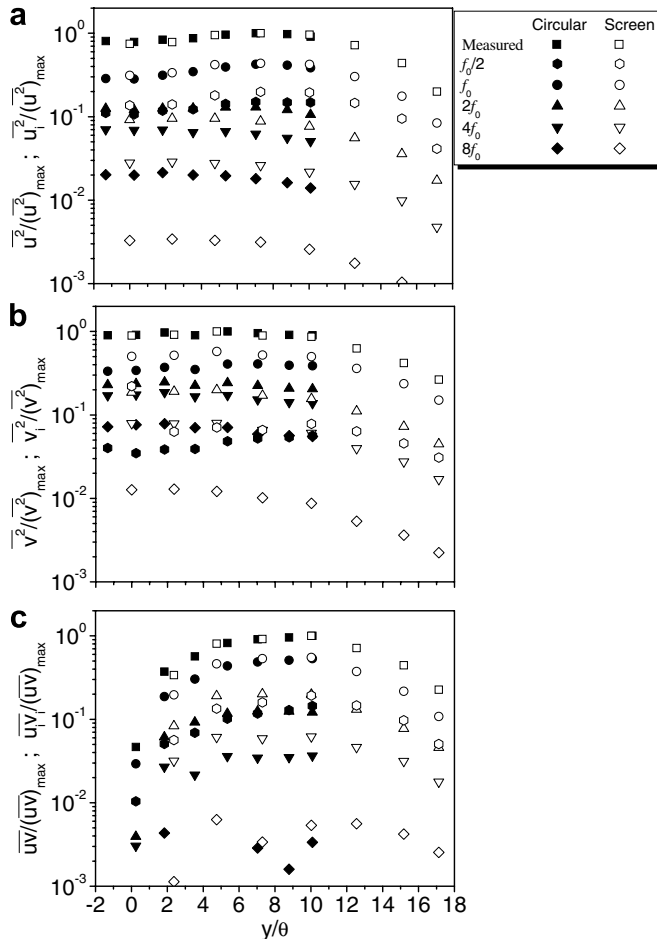

Fig. 12. Velocity variance and shear stress of the measured and the wavelet components at various central frequencies: (a) $\overline{u^2}/(\overline{u^2})_{max}$ and $\overline{u_i^2}/(\overline{u^2})_{max}$; (b) $\overline{v^2}/(\overline{v^2})_{max}$ and $\overline{v_i^2}/(\overline{v^2})_{max}$; (c) $\overline{uv}/(\overline{uv})_{max}$ and $\overline{u_iv_i}/(\overline{uv})_{max}$.
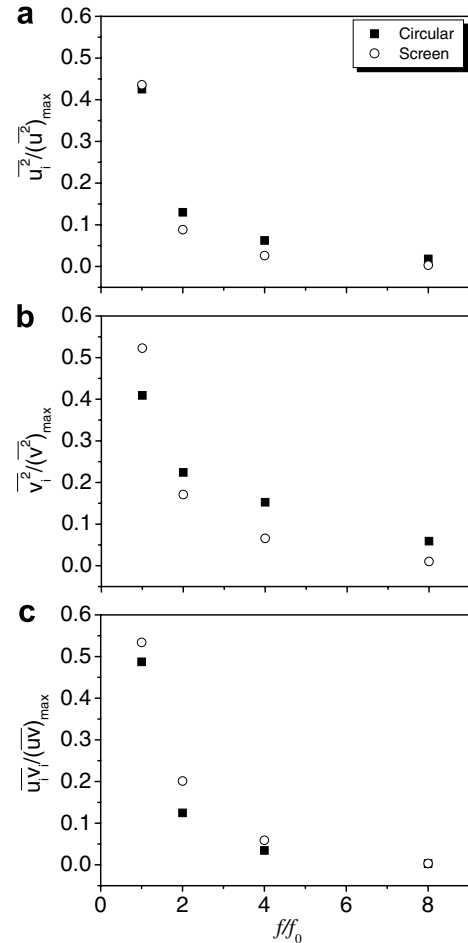
Fig. 13. Dependence of (a) $\overline{u_i^2}/(\overline{u^2})_{max}$, (b) $\overline{v_i^2}/(\overline{v^2})_{max}$ and (c) $\overline{u_iv_i}/(\overline{uv})_{max}$ on the central frequency ($y/\theta \approx 7.0$ for circular cylinder and $y/\theta \approx 7.3$ for screen).

Table 3
Maximum values of $\overline{u^2}/U_1^2$, $\overline{v^2}/U_1^2$, $\overline{uv}/U_1^2$ and $\overline{\omega_z^2}\theta^2/U_1^2$

	$\overline{u^2}/U_1^2$	$\overline{v^2}/U_1^2$	$\overline{uv}/U_1^2$	$\overline{\omega_z^2}\theta^2/U_1^2$
Circular cylinder	0.106	0.064	−0.036	6.3×10^{-8}
Screen	0.098	0.071	−0.033	3.9×10^{-8}

and the contribution from the five components is mostly due to excluding those components of a central frequency below $\frac{1}{2}f_0$.

The maximum value of $\overline{\beta_i\gamma_i}/(\overline{\beta\gamma})_{max}$ corresponding to f_0 is between 40% and 60% of the measured $\overline{\beta\gamma}$, appreciably higher than the maximum coherent contribution (between 20% and 46%) from the large-scale vortical structures, as given in Table 3 of Zhou and Antonia (1995). The vorticity scheme used by Zhou and Antonia (1995) detected the large-scale structures, while the wavelet component of f_0 covers a frequency range from 40 Hz to 140 Hz for cylinder and from 40 Hz to 160 Hz for screen (Table 2). Consequently, it is not surprising to see a difference between the contributions to $\overline{\beta\gamma}$ from the large-scale structures educed by the two techniques.

The $\overline{\beta_i\gamma_i}/(\overline{\beta\gamma})_{max}$ value decreases as the central frequency increases between f_0 and $8f_0$, consistent with the perception that lower frequency eddies contain more energy. When the central frequency increases from f_0 to $2f_0$, the decrease in $\overline{\beta_i\gamma_i}/(\overline{\beta\gamma})_{max}$ is rather rapid, about 28% of $\overline{u^2}$ and 20% of $\overline{v^2}$ for the cylinder but more rapidly for the screen, up to 32% of $\overline{u^2}$ and 40% of $\overline{v^2}$. This indicates predominance in energy by large-scale structures. The appreciable disparity in the decrease of $\overline{\beta_i\gamma_i}/(\overline{\beta\gamma})_{max}$ implies a difference in turbulent structures between the two wakes. Note that in the near wake the contribution to $\overline{u^2}$ and $\overline{v^2}$ from the wavelet component of $2f_0$ is almost the same as that of f_0 for cylinder, though it drops appreciably for screen, exceeding 10%. Evidently, the behaviors of $\overline{u_i^2}$ and $\overline{v_i^2}$ in the far wake bear a similarity to that in the near wake, suggesting a memory of turbulent structures.

The wavelet component $\overline{\beta_i\gamma_i}/(\overline{\beta\gamma})_{max}$ at $2f_0$ is nonetheless significant, ranging between about 10% of $\overline{u^2}$ and 20% of $\overline{v^2}$. A similar percentage is observed in the near-wake of screen (Rinoshika and Zhou, 2005b). In the cylinder near-wake, however, $\overline{\beta_i\gamma_i}/(\overline{\beta\gamma})_{max}$ at $2f_0$ is only marginally smaller than that at f_0, reaching 20% of $\overline{u^2}$ and 40% of $\overline{v^2}$. This probably reflects a difference between the near- and far-wake structures of a cylinder. The maximum $\overline{\omega_z^2}\theta^2/U_1^2$ is 6.3×10^{-8} (Table 3) in the far-wake is much smaller than that (2.0×10^{-6}, derived based on Rinoshika and Zhou, 2005b) in the near-wake. Furthermore, the dominant vortex frequency $f_0 h/U_\infty$ is about 0.2 in the near-wake, but only 0.06 in the far-wake. Namely, the average vortex spacing of the latter triples that of the former. Thus, the vortex stretching is likely weak, which is caused by the interactions between vortices and is largely responsible for the generation of intermediate-scale structures such as longitudinal rib structures. Consequently, the intermediate-scale structures, predominantly longitudinal (Hussain and
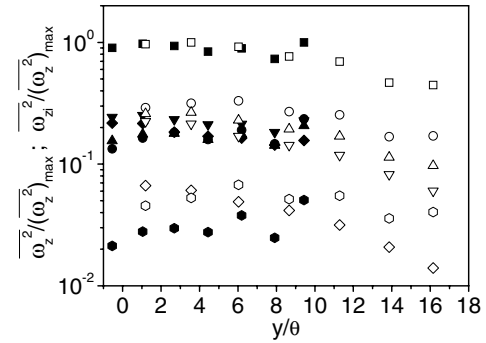

Fig. 14. Vorticity variance of the measured and the wavelet components at various central frequencies. The symbols are the same as in Fig. 12.

Hayakawa, 1987), generated in the saddle region are relatively weak in strength, leading to a less energetic wavelet component at $2f_0$.

The $\overline{\beta_i\gamma_i}/(\overline{\beta\gamma})_{max}$ value of f_0 in the screen wake appears larger than that in the cylinder wake (not so evident in Fig. 12 because of the use of the log scale). The observation conforms to the previous report (Zhou and Antonia, 1995) that the coherent contribution from the large-scale vortical structures to the Reynolds stresses is larger in the screen far-wake than in the solid body far-wake. It further compromises a more rapid decrease in the energy of the wavelet component from f_0 to $2f_0$. The result again confirms the conception that the large-scale vortical structures contribute to the effect of initial conditions on the self-preserving wake. The difference between the two wakes is appreciable down to the wavelet component of $4f_0$, suggesting that the intermediate-scale structures also play a role in the persistence of the initial conditions.

Fig. 14 presents spanwise vorticity variance, $\overline{\omega_z^2}/(\overline{\omega_z^2})_{max}$, and the wavelet components, $\overline{\omega_{zi}^2}/(\overline{\omega_z^2})_{max}$, of $\frac{1}{2}f_0$, f_0, $2f_0$, $4f_0$ and $8f_0$ calculated from Eq. (11). The total contribution from these components accounts for barely 80% of the measured variance. The deficit is due to excluding the wavelet components at a central frequency lower than $\frac{1}{2}f_0$ and higher than $8f_0$, though the effect of the former is probably minor. The component of $\frac{1}{2}f_0$ tends to contribute least in both flows. The $\overline{\omega_{zi}^2}/(\overline{\omega_z^2})_{max}$ value in the screen wake appears decreasing, albeit slowly, as the central frequency increases. This is not so evident in the cylinder wake. Note that $\overline{\omega_{zi}^2}/(\overline{\omega_z^2})_{max}$ corresponding to f_0 is largest, about 30%, among f_0, $2f_0$, $4f_0$ and $8f_0$ in the screen wake. In contrast, $\overline{\omega_{zi}^2}/(\overline{\omega_z^2})_{max}$ at f_0 is smallest, accounting for less than 20% of the total vorticity, among f_0, $2f_0$, $4f_0$ and $8f_0$ in the cylinder wake. Interestingly, a similar difference has been made in the near wake (Rinoshika and Zhou, 2005b). The similarity between the near and far fields is remarkable, further suggesting the memory effect of turbulent structures.

7. Conclusion

The effect of initial conditions on turbulence structures of various scales has been investigated. A vector wavelet

multi-resolution technique is applied to analyse the velocity data obtained in the self-preserving wake behind screen and a circular cylinder, respectively. The data is decomposed into thirteen components based on central frequencies, which are linked with the scales of turbulent structures. The components of the same central frequency, i.e. the same multiple of f_0, are compared between the two flows, leading to the following conclusions.

(1) There is qualitatively little difference in sectional streamlines and spanwise vorticity contours between the turbulent structures of comparable scales in the two flows, though the vorticity level is appreciably larger in the cylinder wake than in the screen one. This is similar to the near-wake observation (Rinoshika and Zhou, 2005b).

(2) The energy of the wavelet component decreases rapidly from f_0 to $2f_0$. The decrease in the screen wake doubles that in the cylinder wake. The observation resembles that in the near wake where the energy of the wavelet component at $2f_0$ is almost identical to that at f_0 for the cylinder, but considerably smaller for screen. In the cylinder near-wake, the large-scale vortical structures are energetic; the intense strain between consecutive vortices is likely to stretch the three dimensional vorticity and generate the structures (Hussain and Hayakawa, 1987) whose strength is comparable with large-scale structures. In contrast, the large-scale vortical structures, probably originating from the mean shear layer instability, in the screen near-wake are relatively weak and are further characterized by large spacing. This may imply a weak strain between consecutive structures. Therefore, the structures at $2f_0$ are not so energetic. The fact that the difference in the strength of turbulent structures at $2f_0$, observed in the near wake, persists in the self-preserving wake implies a memory of turbulent structures.

(3) The wavelet component of f_0 contributes more to Reynolds stresses in the screen wake than in the cylinder wake. The observation conforms to the previous report (Zhou and Antonia, 1995) based on the detections of large-scale structures and compromises

a more rapid decrease in the wavelet component energy from f_0 to $2f_0$ in the screen wake than in the cylinder wake.

(4) As the central frequency increases between f_0 and $8f_0$, the vorticity variance of the wavelet component decreases appreciably in the screen wake, but not so evident in the cylinder wake. Furthermore, $\overline{\omega_{zi}^2}/(\overline{\omega_z^2})_{\max}$ corresponding to f_0 is largest, about 30%, among the components of f_0, $2f_0$, $4f_0$ and $8f_0$ in the screen wake, but is smallest, accounting for less than 20% of the total vorticity, in the cylinder wake, exhibiting a remarkable similarity to that in the near wake.

Appendix A.
Comparison of wavelet multi-resolution analysis with Fourier band-pass filter

For the purpose of comparison, the Fourier band-pass filtering technique is used to analyze the present experimental data. Fig. 15 shows streamlines calculated from the Fourier band-pass-filtered velocity components at the central frequencies f_0 and $2f_0$. The frequency bandwidth applied was the same as when wavelet multi-resolution analysis was used. Some vortical structures at f_0 (Fig. 15a) coincide approximately with those in Fig. 6a, for example, at $tU_c/\theta \approx -47, -16, 5$ and 37. However, others such as those at $tU_c/\theta \approx -36, -4, 4, 14$ and 24 cannot be observed in Fig. 6a. This is because Fourier band-pass filtering technique usually decomposes a signal into components by remaining only a limited range of frequencies,
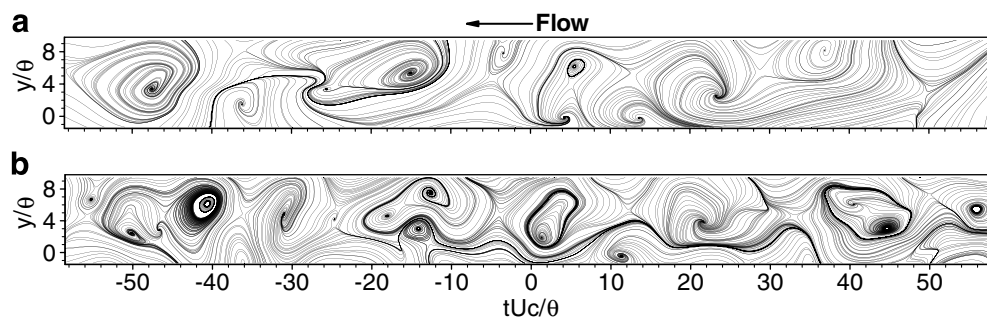

Fig. 15. Fourier band-pass filtered sectional streamlines in the circular cylinder wake: (a) the central frequency = f_0, the frequency bandwidth = 40–140 Hz; (b) the central frequency = $2f_0$, the frequency bandwidth = 80–270 Hz.

covering the entire frequency range of 40–140 Hz. However, the wavelet multi-resolution technique exhibits local characteristics (see its spectrum in Fig. 4a), and extracts only large-scale vortical structures around the central frequency of f_0.

As the central frequency increases to $2f_0$ (Fig. 15b), some structures correspond to those in Fig. 6b, for example, at $tU_c/\theta \approx -41, -31, 2, 20$ and 56. However, others overlap with the structures at f_0 (Fig. 15a), for example, at $tU_c/\theta \approx 12$ and 22. This is because the Fourier band-pass-filtered components are not independent of each other and contain redundant information. Furthermore, the Fourier band-pass filtering analysis is also rather arbitrary in terms of the filter shape and bandwidth (Meneveau, 1991).

In contrast, the wavelet components are independent of each other and do not contain redundant information because the wavelet functions are orthogonal, which cannot be achieved by the Fourier band-pass filtering techniques (Meneveau, 1991; Mouri et al., 1999). It may be concluded that the wavelet multi-resolution analysis provides makes more reliable interpretation of the data.

References

Argoul, F., Arneodo, A., Grasseau, G., Gagne, Y., Hopfinger, E.J., Frisch, U., 1989. Wavelet analysis of turbulence reveals the multifractal nature of the Richardson cascade. Nature 338, 51–53.

Bevilaqua, P.M., Lykoudis, P.S., 1978. Turbulence memory in self-preserving wakes. Journal of Fluid Mechanics 80, 589–606.

Bonnet, J-P., Delville, J., Garem, H., 1986. Space and space–time longitudinal velocity correlations in the turbulent far wake of a flat plate in incompressible flow. Experiments in Fluids 4, 189–196.

Cannon, S., Champagne, F., Glezer, A., 1993. Observations of large-scale structures in wakes behind axisymmetric bodies. Experiments in Fluids 14, 447–450.

Cantwell, B., Coles, D., 1983. An experimental study of entrainment and transport in the turbulent near wake of a circular cylinder. Journal of Fluid Mechanics 136, 321–374.

Cimbala, J.M., Nagib, H.M., Roshko, A., 1988. Large structure in the far wakes of two-dimensional bluff bodies. Journal of Fluid Mechanics 190, 265–298.

Daubechies, I., 1992. Ten lectures on wavelets. Society for Industrial and Applied Mathematics.

Farge, M., 1992. Wavelet transforms and their applications to turbulence. Annual Review of Fluid Mechanics 24, 395–457.

Farge, M., Schneider, K., Kevlahan, N., 1999. Non-gaussianity and coherent vortex simulation for two-dimensional turbulence using an adaptive orthogonal wavelet basis. Physics of Fluids 11, 2187–2210.

George, W.K., 1989. The self-preservation of turbulent flows and its relation to initial conditions and coherent structures. In: George, W.K., Arndt, R. (Eds.), Advances in Turbulence. Springer, Berlin, pp. 39–74.

Giralt, F., Ferré, J.A., 1993. Structure and flow patterns in turbulent wakes. Physics of Fluids 5, 1783–1789.

Hussain, A.K.M.F., Hayakawa, M., 1987. Education of large-scale organized structures in a turbulent plane wake. Journal of Fluid Mechanics 180, 193–229.

Johansson, P.B.V., George, W.K., Gourlay, M.J., 2003. Equilibrium similarity, effects of initial conditions and local Reynolds number on the axisymmetric wake. Physics of Fluids 15, 603–617.

Kiya, M., Matsumura, M., 1985. Turbulence structure in the intermediate wake of a circular cylinder. Bulletin JSME 28, 2617–2624.

Lewalle, J., Delville, J., Bonnet, J-P., 2000. Decomposition of mixing layer turbulence into coherent structures and background fluctuations. Flow, Turbulence and Combustion 64, 301–328.

Li, H., 1998. Identification of coherent structure in turbulent shear flow with wavelet correlation analysis. ASME Journal of Fluids Engineering 120, 778–785.

Li, H., Hu, H., Kobayashi, T., Saga, T., Taniguchi, N., 2002. Wavelet multiresolution analysis of stereoscopic PIV measurements in lobed jet. AIAA Journal 40, 1037–1046.

Louchez, P.R., Kawall, J.G., Keffer, J.F., 1987. Detailed spread on characteristics of plane turbulent wakes. In: Proceedings of 5th Symposium on Turbulent Shear Flows, Lecture Notes in Physics, Springer, pp. 98–109.

Mallat, S., 1989. A theory for multi-resolution signal decomposition: the wavelet representation. IEEE Transactions on PAMI 11, 674–693.

Meneveau, C., 1991. Analysis of turbulence in the orthonormal wavelet representation. Journal of Fluid Mechanics 232, 469–520.

Mouri, H., Kubotani, H., Fujitani, T., Niino, H., Takaoka, M., 1999. Wavelet analysis of velocities in laboratory isotropic turbulence. Journal of Fluid Mechanics 389, 229–254.

Newland, D.E., 1993. Random vibrations, spectral and wavelet analysis, third ed. Longman.

Press, W.H., Teukolsky, S.H., Vetterling, W.T., Flannery, B., 1992. Numerical recipes in FORTRAN (The Art of Scientific Computing), second ed. Cambridge University Press.

Rinoshika, A., Zhou, Y., 2005a. Orthogonal wavelet multi-resolution analysis of a turbulent cylinder wake. Journal of Fluid Mechanics 524, 229–248.

Rinoshika, A., Zhou, Y., 2005b. Effects of initial conditions on a wavelet-decomposed turbulent near-wake. Physical Review E 71 (4, 057504), 1–8.

Wei, T., Smith, C.R., 1986. Secondary vortices in the wake of circular cylinders. Journal of Fluid Mechanics 169, 513–533.

Williamson, C.H.K., 1996. Vortex dynamics in the cylinder wake. Annual Review of Fluid Mechanics 28, 477.

Wu, J., Sheridan, J., Welsh, M.C., Hourigan, K., 1996. Three-dimensional vortex structures in a cylinder wake. Journal of Fluid Mechanics 312, 201–222.

Wygnanski, I., Champagne, F., Marasli, B., 1986. On the large-scale structures in two-dimensional, small-deficit, turbulent wakes. Journal of Fluid Mechanics 168, 31–71.

Yamada, M., Ohkitani, K., 1990. Orthonormal wavelet expansion and its application to turbulence. Progress in Theoretical Physics 83, 819–823.

Zhou, Y., Antonia, R.A., 1993. A study of turbulent vortices in the wake of a cylinder. Journal of Fluid Mechanics 253, 643–661.

Zhou, Y., Antonia, R.A., 1994a. Critical points in a turbulent near-wake. Journal of Fluid Mechanics 275, 59–81.

Zhou, Y., Antonia, R.A., 1994b. Effect of initial conditions on structures in a turbulent far-wake. JSME International Journal Series B 37, 718–725.

Zhou, Y., Antonia, R.A., 1995. Memory effects in turbulent plane wakes. Experiments in Fluids 19, 112–120.

Zhou, Y., Antonia, R.A., Tsang, W.K., 1998. The effect of the Reynolds number on a turbulent far-wake. Experiments in Fluids 25, 118–125.